



**Systematic Uncertainty studies of  
the Crab Pulsar spectrum using the  
LST-1 telescope of the Cherenkov  
Telescope Array Observatory**

**Leonardo Gavira Balmaciz**





# **Systematic Uncertainty studies of the Crab Pulsar spectrum using the LST-1 telescope of the Cherenkov Telescope Array Observatory**

Leonardo Gavira Balmacz

Memoria del **Trabajo Fin de Máster**.  
Máster en Física y Matemáticas (FisyMat)  
Universidad de Granada.

Septiembre 2023

Tutorizado por:

Dr. Rubén López Coto, IAA-CSIC

Dr. Sergio Navas Concha, Dpto. Física Teórica y del Cosmos

**DECLARACIÓN DE AUTORÍA Y ORIGINALIDAD DEL  
TRABAJO FIN DE MÁSTER**

Considerando que la presentación de un trabajo hecho por otra persona o la copia de textos, fotos y gráficas sin citar su procedencia se considera plagio, el abajo firmante D./Dña. Leonardo Gavira Balmacz con DNI 77138479K, que presenta el Trabajo Fin de Máster con el título: Systematic Uncertainty studies of the Crab Pulsar spectrum using the LST-1 telescope of the Cherenkov Telescope Array Observatory

declara la autoría y asume la originalidad de este trabajo, donde se han utilizado distintas fuentes que han sido todas citadas debidamente en la memoria.

Y para que así conste firmo el presente documento en Granada a 02/09/2023

El autor: .....

# Contents

<b>Abstract</b>	<b>1</b>
<b>1 Introduction</b>	<b>3</b>
<b>2 High energy astrophysics</b>	<b>5</b>
2.1 Gamma rays . . . . .	5
2.2 Pulsars as high energy emitters . . . . .	7
2.2.1 Emission mechanisms . . . . .	9
2.2.2 Crab pulsar . . . . .	11
<b>3 Gamma-ray detection</b>	<b>12</b>
3.1 Cherenkov radiation . . . . .	12
3.2 Extensive air showers . . . . .	13
3.3 Ground-based detectors: CTA and LST-1 . . . . .	14
<b>4 Data processing</b>	<b>17</b>
4.1 CTA-lstchain: the software library to process LST-1 data . . . . .	17
4.2 Methodology for the determination of systematic errors . . . . .	24

**ii** SYSTEMATIC UNCERTAINTY STUDIES OF THE CRAB PULSAR SPECTRUM USING THE LST-1  
TELESCOPE OF THE CHERENKOV TELESCOPE ARRAY OBSERVATORY

<b>5</b>	<b>Results</b>	<b>27</b>
5.1	Light curve and reference SED . . . . .	27
5.2	Systematic errors . . . . .	31
<b>6</b>	<b>Conclusions</b>	<b>38</b>
<b>7</b>	<b>Appendix: Statistical expressions.</b>	<b>40</b>

# Abstract

Pulsars are rapidly rotating neutron stars that emit beamed radiation. The high energy radiation emitted by pulsars is measured via ground-based telescopes that detect the Cherenkov radiation emitted by the secondary particles produced in the cascade originated by the primary high energy photon emitted by the pulsar when it enters the Earth's atmosphere. A long processing chain is required to reduce the data to obtain the results that can be used to do science.

In this work we study the systematic uncertainties of the Crab Nebula spectrum using data taken by the prototype Large-Sized Telescope (LST-1) telescope, the first operative telescope of the upcoming Cherenkov Telescope Array (CTA). To determine the systematic uncertainties we vary different analysis parameters and compare their spectral energy distribution to a *reference model*. Firstly, we present the results of the *reference model* used for the comparison, providing a joint fit with the *Fermi*-LAT data. Then, we determine the systematic uncertainties for each analysis parameter and a final total systematic uncertainty of all of them combined. In light of the results, we discuss which analysis parameters or cuts are more influential on the final results. The systematic uncertainties computed will be published in an upcoming article by the Large-Sized Telescope collaboration, together with the first results on the Crab Pulsar obtained by the LST-1.

# Resumen

Los púlsares son estrellas de neutrones que rotan rápidamente a la vez que emiten haces de radiación. La radiación de alta energía emitida por los pulsares se mide a través de telescopios terrestres que detectan la radiación Cherenkov emitida por las partículas secundarias producidas en la cascada originada por el fotón de alta energía primario emitido por el púlsar al entrar en la atmósfera terrestre. Se requiere una larga cadena de procesamiento para reducir los datos y obtener resultados que puedan ser usados para hacer investigación científica.

En este trabajo, estudiamos las incertidumbres sistemáticas del espectro de la Nebulosa del Cangrejo usando datos tomados por el telescopio prototipo Large-Sized Telescope (LST-1), el primer telescopio operativo de la futura red de telescopios Cherenkov Telescope Array (CTA). Para determinar las incertidumbres sistemáticas, variamos distintos parámetros de análisis y comparamos su distribución espectral de energía con un *modelo de referencia*. En primer lugar, presentamos los resultados del *modelo de referencia* usados para la comparación, mostrando un análisis conjunto con datos del satélite *Fermi-LAT*. A continuación, determinamos la incertidumbre sistemática asociada a cada parámetro de análisis y una incertidumbre sistemática total de todas ellas combinadas. En base a los resultados obtenidos, discutimos que parámetros de análisis o cortes son más influyentes en los resultados finales. Las incertidumbres sistemáticas calculadas serán publicadas en un futuro artículo por la colaboración del Large-Sized Telescope junto con los primeros resultados sobre el Púlsar del Cangrejo obtenidos por el LST-1.



# 1 | Introduction

In the Universe surrounding us, there is an astounding number of astrophysical objects constantly emitting radiation with energies in all the electromagnetic spectrum. Most of these emissions (the light emitted by stars, the radiation scattered by cosmic dust, the background microwave radiation) are produced due to the temperature of their emitters. This is what is known as **thermal Universe**. But, there are energies that can not be explained by temperature. Rather, they are caused by collisions between particles and the interaction of charged particles with electromagnetic fields. In this case, we are talking about the **non-thermal Universe**. The most important electromagnetic messengers from the non-thermal Universe are **gamma rays**. To accelerate particles to the highest of energies, the most extreme conditions are needed, which are produced in the vicinity of the most violent objects in the Universe. Such objects include supermassive-black holes with masses million times that of the Sun, or pulsars, dense neutron stars rotating at thousands of times per second.

Much of the non-thermal Universe is still not fully understood. Studying high energy radiation will allow us, firstly, to understand the structure and origin of the extreme objects that produce it. But, additionally, it may shed light on some of the open questions in cosmology and particle physics such as the nature of dark matter. Currently some of these questions are trying to be answered in particle accelerators, but nothing man-made can be compared to the natural acceleration sites that are massive black holes and pulsars. Whilst the Large Hadron Collider (LHC) has reached maximum energies of the order of TeV, these objects constantly emit radiation several orders of magnitude above.

The study of high energy gamma rays is part of one of the newest fields of physics: **particle astrophysics**. This field has seen rapid development since the 2000's thanks to technological advancements made in particle detection. This has resulted in numerous gamma-ray observatories being built around the world. One of such networks of

observatories is the upcoming **Cherenkov Telescope Array** (CTA) [1]. Still under construction, with only one telescope currently operative, this massive array will be the biggest international collaboration studying gamma rays in the next couple of decades. The data collected by CTA will be essential in the study of the most current open topics in physics.

The first CTA operative telescope is the LST-1 [2], located in the Observatorio del Roque de los Muchachos in la Palma, Spain, and has been operative since 2019. One of the objects the telescope has been observing is the **Crab pulsar** [3], a young pulsar merely a 1000 years old, located in the Taurus constellation. The Crab Pulsar is one of the brightest objects in the sky, and due to this it has also been one of the most studied. Such a well known emitter serves as a perfect object to measure with new LST-1 telescope and test its performance.

This said, the detection and analysis of gamma rays isn't a simple task. A long chain of data treatment is needed until proper science can be made from the measurement. During the various steps of this chain, numerous cuts for data discrimination are needed, each of them introducing **systematic errors** to the end result. Characterizing said errors is fundamental so they can be properly adjusted to obtain the maximum quality data after processing.

The main goal of this work is to determine and discuss the systematic bias that certain steps of the data processing chain of the LST-1 telescope introduce. This study will use the most current data on the Crab Pulsar (PSR B0531+21) taken by the telescope. The result obtained in this work will contribute to an upcoming article presenting the latest result on the pulsar. Before presenting the results, we will outline the whole data processing chain of the telescope and the necessary theoretical background needed to understand it.

This document is structured as follows: In Chapter 2 we give an introduction to the field of high energy astrophysics, describing the properties of gamma rays and how they are produced. In Chapter 3 we discuss the mechanisms through which ground-based telescopes are able to detect gamma rays, and we also give an overview of the LST-1 telescope. In Chapter 4 we describe the data processing chain used to process the LST-1 data as well as the methodology followed in this work for the calculation of the systematic uncertainties. The final results of this work together with an in-depth discussion are presented in Chapter 5. Finally, in Chapter 6 we state our final conclusions.

## 2 | High energy astrophysics

### 2.1 Gamma rays

Particle astrophysics, also called high energy astrophysics, is the study of high energy radiation emitted by astrophysical objects. This radiation can come in various forms: charged particles such as protons, electron or heavier nuclei, neutrons, photons and even neutrinos. The first type, charged particles, are referred to as **cosmic rays**, and high energy photons are referred to as **gamma rays**<sup>1</sup>. Out of all the particles arriving at Earth's atmosphere, about 87% are protons, 11% are alpha particles and heavier nuclei and 2% are electrons and photons [4].

Despite making up the majority of high energy radiation, cosmic rays are poor messengers to study the non-thermal Universe. Because they have charge, they are susceptible to interactions with electromagnetic fields that may change their trajectories. When travelling thousands of light years from their origin to Earth, it is very likely that they will get deflected, meaning it is impossible to reconstruct their original source. On the other hand, photons are excellent information carriers, because being neutral particles they do not get deflected, so we know which object emitted them. This is why gamma rays are the preferred particle studied in high energy astrophysics.

The term gamma rays refers to photons with energies above 50 – 100 keV. Depending on their energy, gamma rays can be classified into different ranges:

- Low energy gamma rays (LE)  $E \sim [< 30 \text{ MeV}]$
- High energy gamma rays (HE)  $E \sim [30 \text{ MeV}, 30 \text{ GeV}]$

---

<sup>1</sup>It the literature it is common to see the term "cosmic rays" referring to both charged particles and photons, in this work we will be making the distinction.

- Very high energy gamma rays (VHE)  $E \sim [30 \text{ MeV}, 30 \text{ TeV}]$
- Ultra high energy gamma rays (UHE)  $E \sim [30 \text{ TeV}, 30 \text{ PeV}]$
- Extremely high energy gamma rays (EHE)  $E > 30 \text{ PeV}$

Energies under 1 GeV are mainly of solar origin. The energy range from GeV up to PeV is due to emissions from objects inside our own galaxy, and energies above the PeV are mainly due to extra-galactic sources.

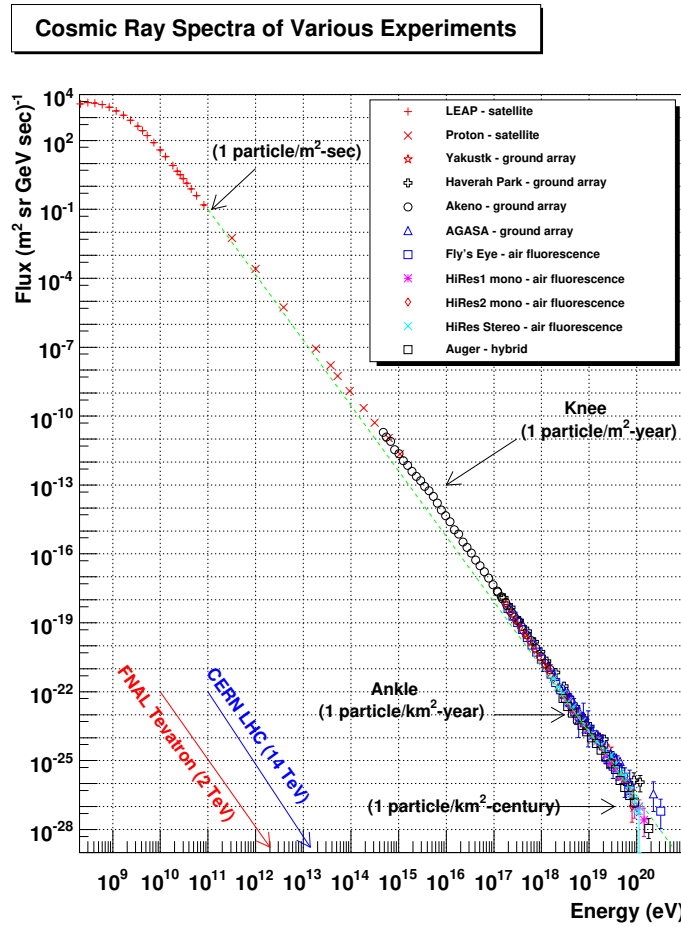


Figure 2.1: Energy spectrum of cosmic and gamma rays. Credit: [5].

The distribution of the energies of cosmic and gamma rays is well described by a power-law  $dN(E)/dE \sim E^{-\Gamma}$ , a straight line when seen in log-scale, as can be seen in Figure 2.1. The spectrum has some well-known features. At  $\sim 3 \times 10^{15}$  eV it has a first break or steepening of the index called the "knee", and at  $\sim 10^{18.5}$  eV it has a flattening

called the "ankle". Up until the knee, the index of the power law is about  $\Gamma \sim 2.7$ , and after it steepens to about  $\Gamma \sim 3.1$  [6]. The knee is interpreted as the change from galactic to extra-galactic sources of emission, although this is still widely discussed [7]. At the ankle, a flattening or decrease of the index is observed. Lastly, at energies  $\sim 10^{19}$  eV, a cut-off is observed. This cut-off is called the GZK cut-off [8, 9], in honor of the physicists who predicted it, and is due to the interactions of the charged particles with the Cosmic Microwave Background.

## 2.2 Pulsars as high energy emitters

To accelerate particles to the above mentioned energies the most extreme environments are needed. There exist broadly two different types of astrophysical objects capable of creating such conditions: Active galactic nuclei (AGN) and Supernova remnants (SNR). AGNs are responsible for most of the high energy radiation of extragalactic origin, whilst radiation from SNRs make up to 90% of the intergalactic cosmic and gamma rays.

Supernova remnants are, as their name suggests, the end products resulting after a supernova explosion. Despite their extreme masses, stars are able to exist without collapsing due to the equilibrium that exists between the inwards gravitational push of the outer shells and the radiation pressure produced by nuclear fusion in the core. But, in really massive stars ( $M > 8M_{\odot}$ , with  $M_{\odot}$  one "solar mass"), this equilibrium breaks. At the end of their lifetimes, massive stars can not produce enough energy in their core to counteract the gravitational push and subsequently collapse. During the collapse the high pressure causes the star to explode ejecting enormous amount of energy and mass, what is known as a supernova.

The mass ejected acts as the shock-wave of the explosion, traveling at high speed and sweeping the surrounding interstellar medium, creating an expanding shell of dust and gas called a **supernova remnant**. At the center of a SNR we can sometimes find a **pulsar** powering the structure.

A pulsar, short for pulsating star, is a neutron star rotating at an extremely high frequency whilst emitting collimated beams of radiation from its magnetic poles. When observed, the intensity of the radiation is the highest when the beams are pointing towards us, acting as a sort of massive lighthouse. This makes it so the star appears to be pulsating, hence its name.

Pulsars are created during the aforementioned collapse of the core of a massive star. Due to the gravitational push of the outer shells, the core is subjected to enormous pressure, raising its temperature. The rise in temperature makes it so electronic capture is favored, a process in which a proton and an electron combine to produce a neutron and a neutrino. The protons and electrons of all the atoms in the core thus combine into neutrons, resulting in an extremely dense mass of degenerate neutrons. A combination of the neutron degeneracy pressure, strong nuclear force and the burst of neutrinos emitted during the capture process halt the collapse of the outer shells, expelling them. Finally, if the remaining neutron core is too massive, it further collapses into a black hole, but if its mass is low enough it stabilizes into a neutron star.

Once stable, neutron stars are extremely small and dense, with radii of around 10 - 20 km and densities of around  $\rho = 5 \cdot 10^{17}$  kg/m<sup>3</sup>. During the collapse, massive stars with masses several times bigger than the Sun's turn into an object just tenths of kilometers in radius. Accordingly, due to conservation of momentum neutron stars rotate with periods of around 1 ms - 1 s. Similarly, due to conservation of the magnetic flux through the surface of the original star, the surfaces of neutron stars have strong magnetic fields, with values around  $B \sim 10^8$  T.

Subjected to these high and rotating magnetic fields, charged particles on the surface of the neutron star are stripped away. The particles can emit photons which are absorbed creating electron-positron pairs. Said electrons and positrons fill the region surrounding the pulsar with leptonic plasma, which co-rotates and alters the magnetic field forming what is known as the **pulsar magnetosphere**.

The plasma subjected to the extreme magnetic field of the plasma makes a perfect environment for particles to be accelerated to the energies observed. The intrinsic geometry of the magnetic field causes the accelerated particles to be emitted along the axis of the poles, resulting in the characteristic beams, also called jets, mentioned above. Additionally, this magnetic axis is not necessarily aligned with the axis of rotation, which explains the pulses observed when the beams point towards Earth. So, in summary, a neutron star that emits jets of radiation along an axis that is not aligned with its rotation axis is known as a **pulsar**. Figure 2.2 shows a schematic image of a pulsar with the rotation and magnetic axis misaligned.

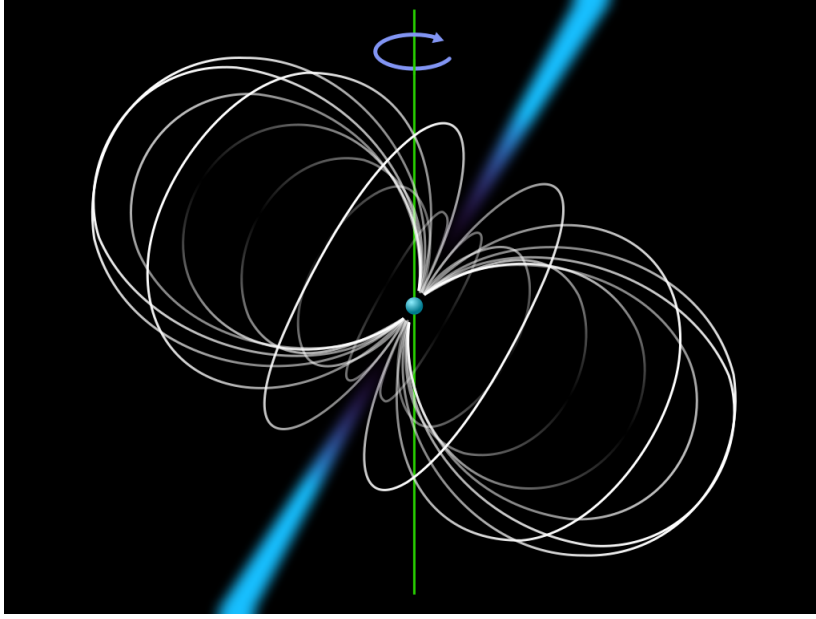


Figure 2.2: Pulsar schematic from [10].

### 2.2.1 Emission mechanisms

We have established that pulsars are the main accelerators causing intergalactic high energy radiation. Knowing their structure, we will discuss the mechanisms that explain the observed gamma-ray spectrum.

Most of the gamma-ray radiation emitted by pulsars is produced by **curvature radiation**. This process, similar to synchrotron radiation, is caused by charged particles (mainly leptons) moving in a curved path, in this the curvature being the magnetic field lines of the pulsar. When moving in this path, the charged particles experience acceleration perpendicular to their velocity and emit radiation. The leptons involved will have a Lorentz factor ( $\gamma$ ) distributed following a distribution  $\mathcal{N}(\gamma) = \frac{dN}{d\gamma}$  dependant on the mechanism of acceleration. Assuming this distribution follows a power-law  $\mathcal{N}(\gamma) \propto \gamma^{-\alpha}$  with a cut-off at  $\gamma_0$ , the energy spectrum of the emitted photons can be approximated as [11]:

$$F(E) \simeq \begin{cases} E^{-\frac{2+\alpha}{3}} & \text{for } E < E_c \\ E^{-\frac{1+\alpha}{2}} \exp\left(-\frac{E}{E_c}\right) & \text{for } E > E_c, \end{cases} \quad (2.1)$$

where  $E_c = E(\gamma_0)$  is the critical energy of the process above which the spectrum has a sharp cut-off. The critical energy is dependent on the Lorentz factor of the particles and the radius of curvature  $r_c$  as following  $E_c \propto \frac{\gamma^3}{r_c}$ . In the above expression we can see that the energy spectrum below the cut-off also follows a power-law  $\mathcal{F}(E) \propto E^{-\Gamma}$  with  $\Gamma = (2 + \alpha)/3$ .

Curvature radiation can explain energies up to the GeV range, but for energies above the tenths of TeV another mechanisms is needed. These energies are obtained via **inverse Compton scattering** (IC). In normal Compton scattering, a photon scatters off an electron at rest. The photon scatters with a certain angle but its energy after the collision is lower than its initial energy. In inverse Compton scattering, the electron is also moving, which means that after scattering the photon energy can be higher than the initial one. Using the assumed power-law for the Lorentz factor of the leptons, the average energy of the photons after scattering is [12]:

$$E_\gamma \propto \begin{cases} \frac{4}{3}\gamma E_0 & \text{if } \gamma E_0 \ll m_e c^2 \text{ (Thomson limit)} \\ \frac{1}{2}E_e & \text{if } \gamma E_0 \gg m_e c^2 \text{ (Klein-Nishina limit)} \end{cases} \quad (2.2)$$

with  $E_0$  being the initial energy of the photon. Accordingly, the energy distribution is:

$$\frac{dN}{dE} \propto \begin{cases} E^{\frac{-\alpha-1}{2}} & \text{if } \gamma E_0 \ll m_e c^2 \text{ (Thomson limit)} \\ E^{-\alpha-1} \ln E & \text{if } \gamma E_0 \gg m_e c^2 \text{ (Klein-Nishina limit)} \end{cases} \quad (2.3)$$

The leptons in the magnetosphere are ultra-relativistic, meaning the spectrum is given by the Klein-Nishina limit. For this process to work, both soft photons and ultra-relativistic leptons (typically electrons and positrons) must be present. The former ones are provided by curvature radiation, giving rise to a conjoint acceleration mechanism known as **synchrotron self Compton**. The process works as follows: first electrons and leptons in the plasma surrounding the pulsar are accelerated to ultra-relativistic velocities. While being accelerated, they emit soft photons via curvature radiation, typically peaking in the X-ray range. These seed photons then interact via IC with their father population of electrons and positrons, gaining energies over the GeV range and in some objects up to the TeV range.

It has to be noted that the processes mentioned above require ultra-relativistic leptons. The acceleration of the leptons depends on the structure and dynamics of the magnetosphere, which is still a widely discussed topic. Different models yield different behaviour for the photon spectrum, specially at its highest ends.

A last remark to be made about the structure of a pulsar is the fact that they lose



energy due to their rotation in the form of electromagnetic radiation. This causes the pulsar to spin-down, meaning its rotational period increases with time.

### 2.2.2 Crab pulsar

The Crab pulsar (PSR B0531+21) is a young pulsar that lies at the center of the Crab nebula (M1), the remnant of supernova SN 1054. The supernova that produced the Crab Pulsar occurred in 1054 and was observed by Chinese and Arab astronomers [13], making it the first deep sky object to be associated with a supernova. The nebula is located  $\sim 6500$  light-years away, in the Taurus constellation at RA:05h 34m 31.94s and Dec:+22°00'52.2" [3]. The Crab Pulsar itself is about 10 km in radius, and weights between 1.4 and 2 solar masses. It rotates with a period of about  $P \sim 33$  ms and has an estimated magnetic field of about  $B \sim 4 \cdot 10^8$  T, making it one of the more energetic pulsars known, with electromagnetic emission throughout the whole electromagnetic spectrum. Its wide spectrum and high luminosity has made it one of the most studied sources in high-energy astronomy, serving as a standard candle of calibration for several missions [14, 15].

The first gamma-ray detections of the Crab pulsar came in the late 1970s. These first measurements [16, 17] confirmed gamma-ray emissions in two distinct pulses in phase with the pulses detected at X-ray and radio energies. The spectrum obtained for this first results followed a power-law. Subsequent observations [18] showed the spectrum until  $\sim 10$  GeV followed a power-law with a spectral index of  $\Gamma \sim 2$  with no evidence of a cut-off, attributed to curvature radiation. The models proposed at the time predicted cut-offs at slightly higher energies, but they were disproved with later detections from ground base telescopes such as MAGIC [19] and VERITAS [20]. Additionally, the *Fermi*-LAT mission also provided better data which gave insight on the 1 – 10 GeV range.

The most recent result published by the MAGIC collaboration [21] reach up to TeV energies. Although there is consensus that emission at these energies has to be due to inverse Compton, the exact acceleration process and structure of the magnetospheric plasma that gives rise to such emission is still widely discussed.

## 3 | Gamma-ray detection

There exist various methods of detecting gamma rays, depending on the range of energies of interest. Historically, the first missions to collect gamma-ray data were orbital satellites, which had the advantage that they could operate outside of the atmosphere. To this day, active orbital missions like the *Fermi-LAT* satellite are still collecting quality data up to hundreds of GeV. But satellite missions have a limit to the maximum energy they can observe. As mentioned in section 2, the energy spectrum for gamma rays follows a power law, meaning that if we increase the energy, the amount of particles emitted by the source quickly decreases. Satellites simply do not have the surface area required to collect sound data at higher energies. Thus, ground base detector are needed.

Ground base detectors have the advantage that they can span wider surfaces, however they have a fundamental drawback: the atmosphere. Fortunately for life on Earth but unfortunately for high energy astronomers, the atmosphere interacts with all the incident high energy particles, causing them to decay before they reach the ground. Because of this, ground based detectors measure the product particles produced when a gamma ray enters the atmosphere via the Cherenkov radiation they emit. There exist two types of **Cherenkov detectors: air based** and water based. We will be focusing on the former ones.

### 3.1 Cherenkov radiation

Cherenkov radiation is a type of radiation produced when a charged particle moves in a medium with velocity higher than the speed of light in this medium (in mediums other than vacuum this is possible). When a charged particle is moving through a dielectric medium with refractive index  $n$ , it polarizes the molecules of the medium,

exciting them. The excited molecules re-emit the excess of energy as an electromagnetic wave which will propagate forming spherical wave fronts with speed  $c/n$ , where  $c$  is the speed of light in vacuum. The emitted wave front will originate from the point of the trajectory of the charged particle. If the speed of the particle is greater than that of the radiation  $v_p > c/n$ , the wave front will interfere forming a light cone along the particles path (see Figure 3.1).

This cone will form an angle of

$$\cos \theta_c = \frac{1}{n\beta} \quad (3.1)$$

with respect to the direction of the particle. This light, although too faint to be seen with the naked eye, can be measured by detectors. Due to the high energies at play when cosmic and gamma rays enter the atmosphere, the wavelength of the Cherenkov radiation they produce peaks around the ultraviolet.

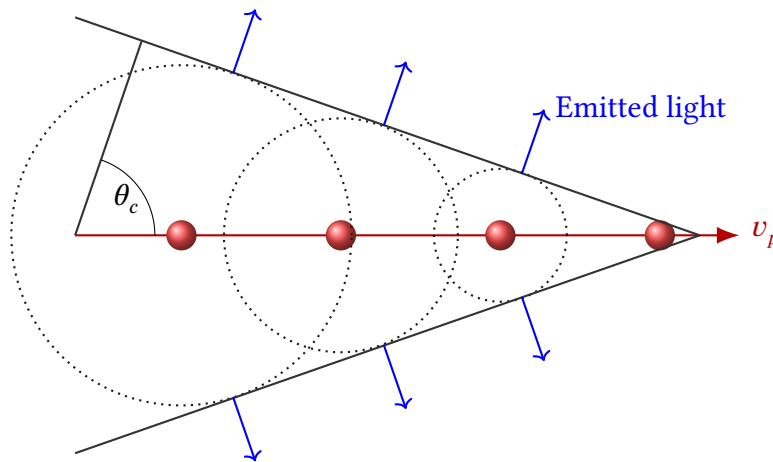


Figure 3.1: Schematic illustration of the Cherenkov effect. In this image  $\theta_c$  is angle of the light cone respect to the particles path and  $v_p$  the velocity of the particle.

## 3.2 Extensive air showers

When high energy particles enter the atmosphere, they interact with the air molecules via several different emission or disintegration processes. The resulting products of these processes still carry enough energy to further interact with the atmosphere, producing more particles. This chain continues in what is called a **extensive air shower**.

At each step in the shower the number of particles increases and the average energy of each one decreases. The end product and the geometry of the shower depend on the initial particle type and energy. We can distinguish between two types of air showers: hadronic air shower and electromagnetic air showers.

**Electromagnetic air showers.** These showers are produced when the primary particle that enters the atmosphere is either a photon or an electron. When a high energy photon or an electron enter the atmosphere, they are subjected to the electric field that the atoms in the air create. This inhibits pair photo-production, a process in which the photon decays into an electron-positron pair. These secondary leptons in presence of the electric fields created by the atoms, emit photons via bremsstrahlung. The photons emitted this way in turn decay into more electron-positrons continuing the cascade. Due to the nature of the processes involved, these showers tend to be narrow.

**Hadronic showers.** When cosmic rays (mainly protons) enter the atmosphere, they initiate hadronic showers. In these showers, the particles interact electromagnetically but also via the strong force. This makes it so these showers have more fluctuations in their end products compared to electromagnetic ones, and due to the masses involved they have a wider lateral extent. The main products of hadronic showers are pions, kaons, muons and nucleons. There are three types of pions:  $\pi^+$  and  $\pi^-$  which are charged particles, and a neutral  $\pi^0$ . Because the  $\pi^0$  has no charge, it can decay into two photons, which can initiate electromagnetic showers. This means that about one third of a hadronic shower is of electromagnetic nature, and hence emits Cherenkov radiation. Examples of both types of showers can be seen in Figure 3.2.

### 3.3 Ground-based detectors: CTA and LST-1

Ground-based experiments are designed to detect Cherenkov radiation emitted by the charged particles produced in the air showers. From the collected photons, after an extensive chain of data processing, scientists are able to reconstruct the physical parameters of the incident particle.

The Cherenkov Telescope Array (CTA) [1] will be the next generation of telescopes used for high energy astronomy. Currently under construction, the final ensemble will be constituted by more than 100 telescopes distributed between two networks, one in the northern hemisphere and one in the southern hemisphere. The

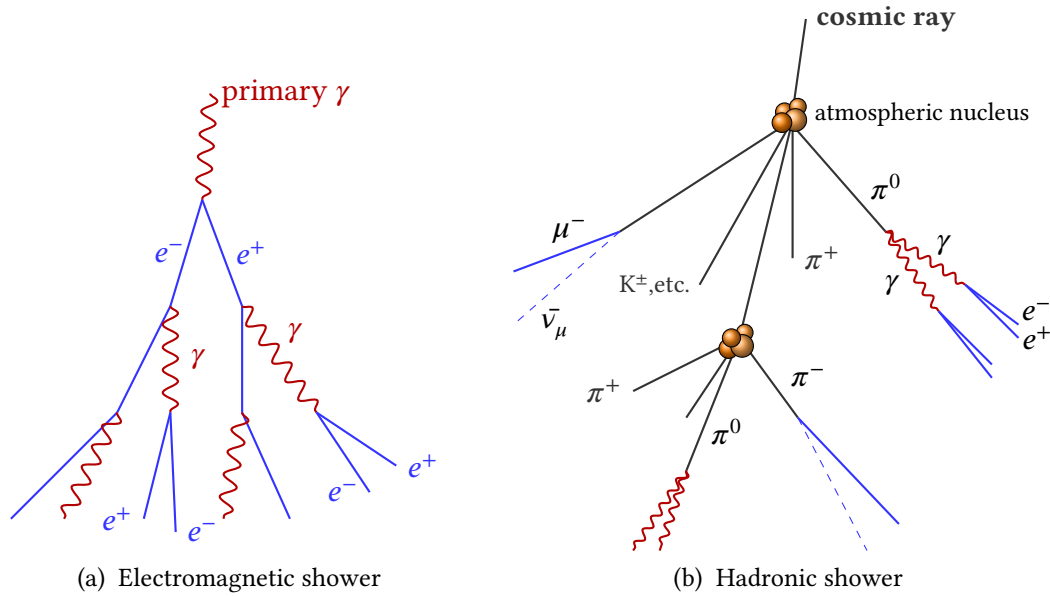


Figure 3.2: Schematic drawing of an electromagnetic shower (a) and a hadronic shower (b).

northern array (CTA North) will be located in the Observatory Roque de los Muchachos, in La Palma, Spain, and will cover energies from 20 GeV to 5 TeV. It will span an area of about 1 km<sup>2</sup>, making it the smaller site. The southern site (CTA South) will be located in Paramal, Chile, and will detect energies from 150 GeV to 100 TeV. To cover the wide range of energies proposed, CTA will work with three different telescope designs with different sizes and sensitivities: Large Size Telescopes (LST), Medium Size Telescopes (MST) and Small Size Telescopes (SST).

In 2018 the construction for the first prototype LST was completed, the **LST-1**. In this TFM we will be using data collected with this telescope, meaning we are working with the latest data on high energy gamma rays collected by a state-of-the-art Cherenkov telescope.

The LST-1 is composed by a 23 m diameter reflective parabolic surface, spanning about 400 m<sup>2</sup> (see Figure 3.3), that channels the Cherenkov light emitted during showers to a detector formed by 1855 photomultipliers divided into 265 tubes. The telescope is 45 metres tall and weights 100 tonnes, but is able to reposition itself in only 20 seconds. The telescope can detect energies from 20 to 150 GeV so it will focus mainly on galactic sources and active galactic nuclei with high red-shift.

The Cherenkov photons emitted by the showers arrive at the mirrors of the parabolic

**16** SYSTEMATIC UNCERTAINTY STUDIES OF THE CRAB PULSAR SPECTRUM USING THE LST-1 TELESCOPE OF THE CHERENKOV TELESCOPE ARRAY OBSERVATORY

surface, which reflect the photons into the camera. In the camera, the photons are detected by the photomultipliers where, via photoelectric effect, an electron is emitted. The electron initiates a cascade of electron that create a current that is measured and turned into an electric signal which can be digitalized. So, the individual photons are turned into digital signals which are used to create the images of the Cherenkov flash. Each of the 1855 photomultipliers corresponds to a pixel in the digital image.



Figure 3.3: Image of the LST-1. Credit [22].

Working on the LST project there are more than 300 scientist and engineers from 12 different institutions in 30 countries. The results on the first measurements were published in 2021 [2], with follow up articles about the general performance and other observations came shortly after [23, 24].

## 4 | Data processing

### 4.1 CTA-lstchain: the software library to process LST-1 data

From the detection of the Cherenkov radiation to the reconstruction of the physical parameters of the incident particle, a long data processing chain is required. For LST-1, this chain called the LST-chain [25]. This chain is written in python. In this section, we will outline the various steps or data levels in the chain. The basic structure is as following: the raw data measured by the telescope arrives at data level R0. The raw data is then processed through data levels R1, DL0 and D1a until a cleaned image of the Cherenkov flash is obtained. The next step is DL1b, where certain significant parameters are obtained from the image. These parameters (like the intensity or center of the flash) are then used in DL2 to reconstruct important quantities like the energy or the type of the particle. This reconstruction is done by Random Forest algorithms that are trained with Monte Carlo (MC) simulations. Based on these quantities, a list of possible gamma rays are selected. This list, together with Instrument Response Functions (IRFs) of the telescope form the next data level DL3, which can be used to obtain the final results used in meaningful science. A schematic of the chain with the different python packages it uses can be seen in Figure 4.1. In this figure, the upper branch shows the processing pipeline of the MC simulations. We can see how the simulations are split into two batches, the ones used for training the Random Forest algorithms and the ones used to determine the IRFs. The lower branch shows the processing of the real data:

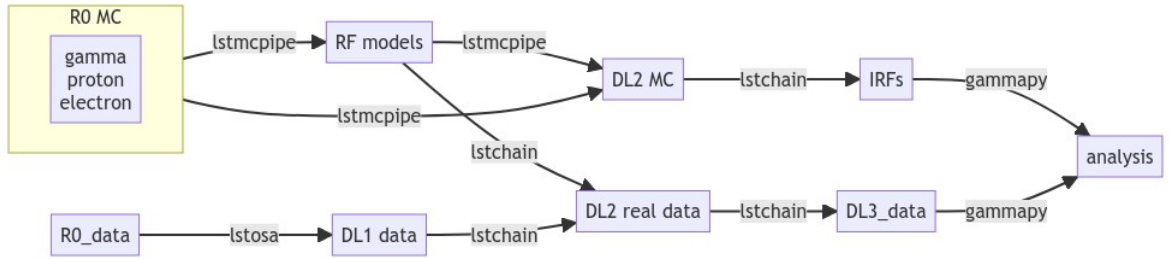


Figure 4.1: Schematic overview of the LST analysis pipeline. Credit: [26]

Out of these levels, we are interested in data levels DL2 and beyond, as it is in these levels where the systematic errors we study are produced. A more detailed description for each data level is given below.

### Data levels R0 to DL1a.

Each camera **event** of raw data collected by the telescope consists of two  $\sim 40$  ns movies, one of them for the high gain the other for the low gain of the photomultiplier. Each movie is a sequence of 40 consecutive samples or images taken with 1 ns exposure time that captures the light emitted by one Cherenkov cascade. Observation of a source with LST-1 are carried out in *runs* or time intervals of 20 minutes. So, a run contains all the events detected during that 20 minute period. A first preliminary selection process discards runs with unfavourable weather and/or moon conditions. The raw data arrives in `zfits` format.

The next step, R1, is properly calibrating the movies. Once calibrated, the frames of the movie can be integrated into two images for each event. For the integration, normally only the high-gain movie is used. Out of the two images obtained after integration, the first one captures the light deposited in the camera measured in photo-electrons (p.e.) and the second one captures the activation time of each pixel in ns. The next step is cleaning the image, this means removing irrelevant pixels and noise to reduce the image to the relevant pixels that capture the Cherenkov light emitted by the shower. After this process the data is stored in `hdf5` format.

### Data level DL1a to DL1b.

After cleaning, the images are parameterized by a set of key values know as the Hillas parameters [27]. The idea behind this parametrization is that the gamma-ray pictures on the focal plane can be approximated by ellipses (see figure 4.2). Following this consideration, the images can be characterised by the features of the ellipse plus



higher order moments. This way, instead of working with the images themselves we work with a set of values from which information of the incident particle can be reconstructed, greatly reducing computational cost. The list of Hillas parameters used in the analysis is the following:

- **Log intensity.** The decimal logarithm of the intensity, the sum of the charges of the pixel images that survived after the cleaning process. All other parameters below are calculated using the same set of pixels.
- **Width, length** and **wl.** The width and length of the ellipsis, computed as the second moment of the distribution along the mayor and minor axis, and the width to length ratio, wl.
- **Center coordinates.** The (x,y) coordinates on the image of the center of the ellipsis.
- **Skewness** and **kurtosis.** The skewness (third moment) and kurtosis (fourth moment) of the distribution.
- **Time gradient.** Gradient of time of the signal arrival, computed along the main axis.
- **Leakage intensity width.** Fraction of the total charge of the image that is recorded at the border of the image or near it.
- **Azimuth** and **altitude.** The pointing direction of the telescope at the time of detection.

### Monte Carlo simulations and Random Forest.

The physical parameters of interest can not be directly obtained from the Hillas parameters mentioned above, in the sense that there is no formula or equation relating them. Instead, Random Forest algorithms are trained to reconstruct the physical parameters based on the Hillas values. To train these algorithms, detailed Monte Carlo simulations are needed. Additionally, MC simulations are also used to determine the Instrument Response Functions of the telescope.

Extensive air showers are simulated in detail from their origin in the top of the atmosphere to the digitization of the signals recorded by the camera trigger system, resulting in movies completely equivalent to those obtained from real data. This includes simulating the various steps of detection with the telescope, like the reflection of the Cherenkov light or the passage through the camera entrance so that the IRFs may be determined. All the steps are simulated taking into account laboratory measured performance of the various elements involved. The movies obtained by the

simulations can be then treated using the steps outlined above until the calculation of Hillas parameters, but in this case we know the original energy, direction and type of particle that gave rise to these parameters. Random Forest algorithms can be trained using this information so that given the Hillas parameters of a real event they can classify it and reconstruct its physical parameters.

We can distinguish between two batches of simulations. On one side, the **training MC**, used for the training of the Random Forest reconstruction algorithms. On the other side, the **test MC**, which are processed using the already trained algorithms to later determine the IRFs. For the training MC, simulations are performed for incident photons, electrons and protons. This is done so the algorithms learn to differentiate between the different types of particles. The training MC are simulated along different points or **nodes** spaced equally along declination lines. For the **test MC**, only gamma rays are simulated and the simulations are carried out over 12 nodes, different of the ones used for training.

### **Data level DL1b to DL2.**

The next step in the data processing chain is to use the algorithms trained with MC simulations to reconstruct physical parameters of interest of the real DL1b data. The reconstructed parameters are: energy and direction of the primary particle and *gammaness*, a score that indicates how likely is that the particle is a gamma ray. Certain Hillas parameters are more or less significant depending on the reconstructed quantity.

The reconstruction of the position would ideally be stereoscopic, i.e. based on the simultaneous detection of various telescopes located at in different positions. Unfortunately, the LST-1 operates alone at the moment so the reconstruction needs to be source-dependent. In this type of analysis, the position of the source of the gamma rays is assumed to be known. When applying this to MC simulations, to characterize the reconstructed position, the angle  $\alpha$  (see Figure 4.2) is defined as the angle between the mayor axis of the ellipse and the line that connects the center of the ellipse to the assumed position of the source.

### **Instrument Response Functions.**

After being trained, the Random Forest models are also applied to MC simulations on the testing nodes, to determine the IRFs of the telescope in those directions. IRFs are used to measure the performance of the LST-1 telescope as a function of energy and pointing direction, and are used in conjunction with the real data in further stages

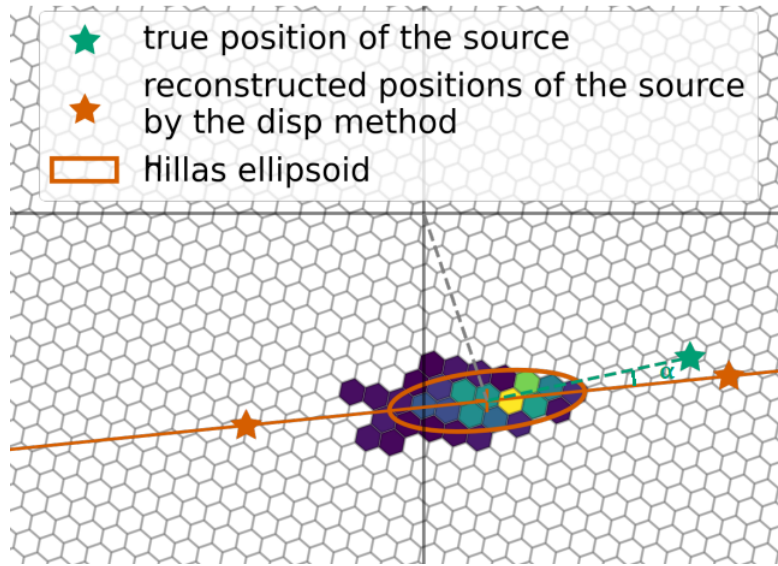


Figure 4.2: Hillas ellipse of a Chereknov flash.

of the analysis. Before the calculation of the IRFs, certain cuts are applied depending on the energy, reconstructed position and type of particle. A relative energy resolution can be defined to measure how well the energy of the particles is reconstructed:

$$\frac{|E_R - E_T|}{E_T} = \frac{|\Delta E|}{E_T}, \quad (4.1)$$

where  $E_R$  is the reconstructed energy of the MC simulated shower and  $E_T$  is true energy.

The first cut to be applied is a global cut in intensity. The second is a energy dependant cut in *gammaness* or **gamma/hadron efficiency**. The cuts applied are so that only a percentage of the best *gammaness* are kept. So for example a cut of 70% in g/h efficiency means that only 70% of the particles with best *gammaness* are kept. Similarly, another cut that is applied is called **alpha containment**. This cut, similar to the cut in energy efficiency, keeps a percentage of particles with the best reconstructed  $\alpha$  angles. The quality of reconstruction for  $\alpha$  is given by a analogous expression to equation 4.1. If more relaxed cuts are applied, we keep more particles which gives better statistics, but at the risk that the parameters are not well reconstructed. On the other hand, tighter cuts give less statistics but better reconstruction. It is thus important to find a value for the cut which balances out both ways.

### Data level DL2 to DL3.

For the creation of the DL3 files of the real data, a global cut in *gammaness* is applied to the events. This is done to filter cascades produced by hadrons. Then, out of the parameters contained in the DL2 files, only the relevant ones for further analysis are kept, mainly the reconstructed energy and position, the time of arrival and the pointing parameters of the telescope. Depending on the final analysis to be performed, some additional parameters may be stored. Summing up, to this point we have two different types of files: DL3 of real data, containing a few important parameters, and IRF files for each node in the sky. For further analysis we have to remind that the IRFs are not computed for the whole sky, but rather for a few nodes. As such, the real event contained in the DL3 files are assigned to their closest node so that the proper IRF may be applied. The process of generating the IRFs and the process from DL2 to DL3 are controlled via configuration files. Both DL3 data and IRFs are stored in FITS format.

In Listing 4.1 we show an example of the configuration files used to vary the different analysis parameters used in the step from the DL2 to DL3 stage. Firstly we can see that flat cuts are applied for both the reconstructed trajectory of the particle and its *gammaness* (gh efficiency in the configuration file). Then, the two percentage cuts alpha containment and g/h efficiency described above are applied.

Listing 4.1: Configuration file example for DL2 to DL3

```
{
  "DL3Cuts": {
    "min_event_p_en_bin": 100,
    "min_gh_cut": 0.1,
    "max_gh_cut": 0.95,
    "min_alpha_cut": 1,
    "max_alpha_cut": 20,
    "fill_alpha_cut": 20,
    "alpha_containment": 0.7,
    "gh_efficiency": 0.7,
    "allowed_tels": [1]
  }
}
```

### Data level DL3 to DL3pulsar.

This is an intermediate step before the higher stages of the analysis. The DL3 data is reduced to a spectrum data-set. This means reducing the data into a 1D count spectra. This reduction is performed on each run individually, as they are dependant

on the IRFs and other parameters of the observation. The DL3pulsar files are stored in OGIP format files.

Because the number of photons arriving at each pulse is extremely low, gamma rays coming from the same region are summed over and properly averaged. But, to perform this summation correctly, we need a model of rotation of the pulsar to properly time the events. This model of rotation has to take into account the fact that the pulsars spins-down, lowering its frequency. This frequency at a time  $t$  can be expressed as a Taylor expansion:

$$\nu(t) = \nu_0 + \dot{\nu}_0(t - t_0) + \frac{1}{2}\ddot{\nu}_0(t - t_0)^2 + \frac{1}{6}\dddot{\nu}_0(t - t_0)^3 + \dots \quad (4.2)$$

The set of estimated parameters  $(\nu_0, \dot{\nu}_0, \ddot{\nu}_0)$  is called a *pulsar ephemeris* at time  $t_0$ . The ephemeris for the Crab Pulsar are obtained from the Jodrell Bank Observatory monthly updates ephemeris [28, 29].

The pulsar phase  $\phi$  is defined as the number of turns it has completed since the reference time  $t_0$ . This phase can be divided into discrete bins, and a histogram called a *phaseogram* can be made representing the number of events in each bin. The phaseogram can give information about the different emission regions of the pulsar, as well of the geometry of these regions. Keeping up to-date ephemerides is essential, specially when working with extensive data-sets spanning over large periods of time. Proper timing of the events ensures that they are binned correctly and no information on the phaseogram is lost. In this step a last cut in zenith distance (zd) is applied.

#### DL3pulsar to DL4.

This is the final level of data analysis, where the final result used for proper science are obtained. For this stage of the analysis a different repository [30] is used. This repository depends on functions of `lstchain` as well as `gammapy` [31].

Firstly, using the reduced spectrum data-set properly timed by ephemeris the light curve or phaseogram can be computed. Then, all the data sets are stacked together so that a likelihood fit can be performed according to an input model. Finally, **flux points** are estimated. These points are estimated by fitting the amplitude of reference model only to the point inside pre-defined bins. The amplitude is the normalized according to the amplitude of the model [32].

The flux point and best-fit model are represented in a Spectral Energy Distribution (SED). In this plot, the differential energy flux  $\left(E^2 \frac{dN}{dEdtdA} = E^2 \frac{d\Phi}{dE}\right)$  is plotted versus energy, both in logarithmic scale.

## 4.2 Methodogy for the determination of systematic errors

In this section we will explain the methodology followed for the determination of the systematic errors, specifically the systematic errors regarding the Spectral Energy Distributions. The first step is selecting a *reference model*, a set of data whose SED fit parameters will be the ones we use to study variations. Once the reference model is set, we generate data for different cuts and compute their SED fit parameters. Comparing the parameters of the different cuts with the reference one we obtain the systematic error associated to that cut.

For the data generation, we always start from the DL2 data level. This means all the subsequent higher level generated data, starts from the same parameterized image, and the difference lies in the cuts applied in the later stages of the analysis. The cuts applied for the reference model are: alpha containment = 70%, energy efficiency = 70%, zenith distance = 50°, intensity leakage = 100%. For the intensity cut, two different cuts were applied depending on the date the data was taken. Due to changes in the telescopes camera performance, data taken before August 2021 has a intensity cut of 80 p.e. and data taken after has a cut on 50 p.e. The different data-sets were generated by processing DL2 data and varying always one cut at the time. The different analysis parameters generated are:

- Gamma/Hadron efficiency: 50%, 60%, **70%**, 80%, 90%.
- Alpha containment: 50%, 60%, **70%**, 80%, 90%.
- Zenith distance: 30°, 40°, **50°**, 60°, 70°.
- Intensity cut: **80 p.e.** (before August 2021), **50 p.e.** (after August 2021), 100 p.e.
- Intensity leakage width: 20%, 50%, **100 %**.

For all cuts above, we carried out the analysis from DL2 onward until we obtained the best-fit parameters of the SEDs. All the cuts with exception of the cuts in the zenith distance are applied in the step from DL2 to DL3. This means that they also require new IRFs to be generated so that the SEDs can be correctly determined. The values of the analysis parameters generated are such that all of them could be used for proper science. A cut of, for example, 20% in gamma/hadron efficiency is too restrictive and would realistically never be applied if the Spectral Energy Distribution of the pulsar wanted to be studied. So, we do not consider such extreme values of the analysis parameters as they would give an over estimation of the systematic uncertainty.

Once all the fit parameters have been extracted, we compare then with the reference fit. For each possible cut, we have a number of fits for different values of these cut, e.g. for alpha containment we have fits for 50%, 60%, etc. Out of all the fit parameters for a certain cut, we select the maximum and minimum value for each parameter. These values will give us a lower error and an upper error for the cut. Both the upper and lower error are calculated according to:

$$\epsilon_{cut,\beta} = \frac{\Delta\beta}{\beta_{ref}} = \frac{|\beta_{cut} - \beta_{ref}|}{\beta_{ref}}, \quad (4.3)$$

where  $\beta$  is the fit parameter we are calculating the error for. Because we have an asymmetric error interval, instead of expressing the parameters in the form  $\beta \pm \Delta$  they will be expressed as  $\beta_{-\Delta_{lower}}^{+\Delta_{upper}}$ . The exception to this method is the cut in intensity. The cuts applied in the reference model for intensity were estimated as the lowest possible taking into account the camera performance, so applying lower cuts made no sense. Thus, only a upper cut was applied and its error serves as symmetric error. Using the computed values we also plotted the SED of the reference fit with error regions corresponding to the systematic errors of each cut.

Additionally, we also computed the total systematic error due to all the cuts in conjunction. To compute it, we summed all the error via quadrature:

$$\Delta_{systematic} = \sqrt{\Delta_{energyeff.}^2 + \Delta_{alphacont.}^2 + \dots}, \quad (4.4)$$

and we plotted the total error region due to systematic errors.

We also examined the associated error to each sky node for which the IRFs are calculated. This required calculating the fit parameters using only the events assigned to each node, and computing the deviation with respect to the reference model.

For all of the processes mentioned in this section, new programs in python were developed. This includes an implementation to loop over different cuts in the software used from DL2 to DL4 including IRF creation, and programs to extract the parameters and compute and represent the systematic errors from the generated data.

In Listing 4.2 we show a snippet of the code used to determine the systematic errors. Firstly, we read the best-fit parameters for all of the values generated for alpha containment, which have been previously computed and saved in cvs format. Then, we compute the upper and lower errors. To to this we select the maximum and minimum value out of the list of parameters and calculate the difference respect to the values of the *reference model* (`spectra_P1.model_best` in the snippet).

Listing 4.2: Code snippet for the determination of systematic errors.

```
index_list_P1alpha = []
amp_list_P1alpha = []

for file in files_P1_alpha:
    df = pd.read_csv(file)
    index_list_P1alpha.append(df['value'][0])
    amp_list_P1alpha.append(df['value'][1])

index_max_P1_alpha = np.abs(np.max(index_list_P1alpha) -
spectra_P1.model_best.parameters.to_dict()[0]['value'])
index_min_P1_alpha = np.abs(np.min(index_list_P1alpha) -
spectra_P1.model_best.parameters.to_dict()[0]['value'])
amp_max_P1_alpha = np.abs(np.max(amp_list_P1alpha) -
spectra_P1.model_best.parameters.to_dict()[1]['value'])
amp_min_P1_alpha = np.abs(np.min(amp_list_P1alpha) -
spectra_P1.model_best.parameters.to_dict()[1]['value'])
```

We also perform a joint fit using the LST-1 data together with data from the *Fermi*-LAT telescope [33]. The *Fermi*-LAT data is processed to the DL4 level and required no prior treatment. We then join both data sets together and perform different fits using *gammapy*.



# 5 | Results

## 5.1 Light curve and reference SED

The central point of our analysis is a set of processed reference DL4 data, which we will use to compare how the different variations in the analysis parameters affect the results. In this section, we will introduce the full results obtained from analysing the reference data. The aim of this section is to give insight on the final results obtained after the chain of data processing, as well as contextualising how they are used to obtain information about the pulsar.

In Figure 5.1 we show the resulting phaseogram obtained using 103.6 hours of observation. From the morphology of the phaseogram we can observe two clearly differentiated peaks, **P1** and **P2**, detected with significances of  $10.8\sigma$  and  $12.7\sigma$  respectively. The peaks P1 and P2 are defined in terms of the pulsar's rotational phase. Each peak has an associated interval or phase range. If an event is detected with the pulsar's phase being in one of those intervals, it counts towards the statistics of the corresponding peak. The phase ranges for the peaks are defined as **P1**:  $[0, 0.026, 0.983, 1]$ , **P2**:  $[0.377, 0.422]$ . An **OFF** region is considered in phase range  $[0.52, 0.87]$  used to estimate the background. These three regions have been defined according to the MAGIC 2016 publication on the Crab Pulsar [34]. Additionally, a fourth region with significant emission between the two peaks has been detected with significances of  $6.1\sigma$ . This region is called the **bridge** (**P3** in figure 5.1) defined in the MAGIC article about the bridge emission of the Pulsar [35].

The significance with which the three regions P1, P2 and the bridge have been detected is in good accordance with measurements from other telescopes in the 10 – 100 GeV range [36, 34, 35]. This serves as proof of the efficiency of the LST-1 telescope and its data analysis pipeline.

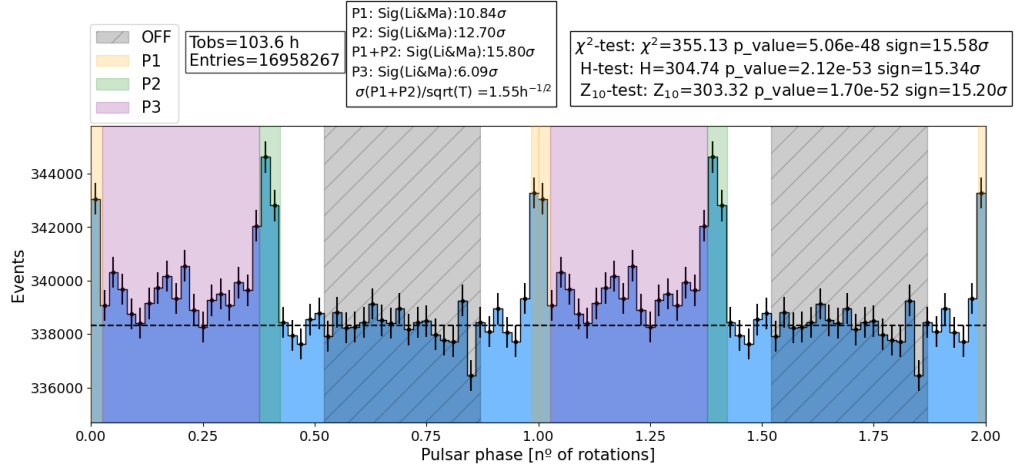


Figure 5.1: Phaseogram for the Crab pulsar with 103.6 hours of observation and a total event count of 16958267. The peak regions P1 and P2, the bridge region P3 and the OFF region are highlighted and their significances are given. Three different statistical test are shown with their respective p-values. The p-values of the test are low enough to reject the null-hypothesis.

We can also note that the width of P2 is higher than that of P1, meaning more photons arrive from this region in the range of energy detected. Previous results studying the ratio P2/P1 between both peaks at lower energies [35, 37, 38] show this ratio is energy dependent and increasing, meaning that P1 emits more in lower energies whilst P2 emits in higher energies. This behaviour, as well as the existence of the bridge are topics still widely discussed among the scientific community.

Regarding the spectral analysis, in Figure 5.2 we show the SEDs for the reference data with its corresponding fits. For P2, seven spectral points were computed. For P1, only six were due to lack of data data at higher energies.

Both peaks can be fitted according to a power law of the form:

$$\frac{d\Phi}{dE} = \Phi_0 \left( \frac{E}{E_0} \right)^{-\Gamma} \quad (5.1)$$

In the fits,  $E_0$  has a fixed value of 30 GeV for P1 and 40 GeV for P2. These energy reference values, called decorrelation energies, are determined to minimize the correlation between the flux normalisation and the spectral index.

The best-fit parameters obtained for both peaks, and thus, the reference parameters are summarized in Table 5.1:

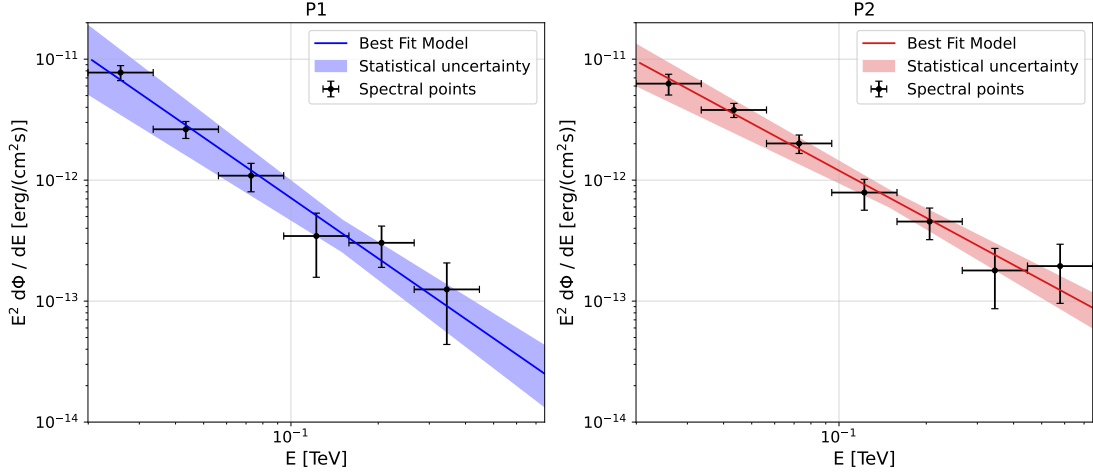


Figure 5.2: SEDs with best-fit reference models.

Peak	$\Phi_0[\text{cm}^{-2} \text{s}^{-1} \text{TeV}^{-1}]$	$\Gamma$	p-value
P1	$(1.1 \pm 0.3) \cdot 10^{-11}$	$3.66 \pm 0.17$	0.0007
P2	$(1.1 \pm 0.3) \cdot 10^{-11}$	$3.29 \pm 0.11$	0.0003

Table 5.1: Fit parameters of the reference model.

The low p-value for both fits confirms their validity. We can observe how the spectral index for P1 is steeper than that of P2, yielding a difference of  $\Gamma = \Gamma_1 - \Gamma_2 = 0.4 \pm 0.2$  meaning at higher energies the flux of particles will be smaller. The fact that the P2 is detected with better statistics will also come into play in the discussion below regarding the systematic errors. This behaviour has been confirmed by observations in the X-ray range and above. It has to be noted that the index of the power law varies along different energy ranges. For the NuSTAR data the indices are  $\Gamma_1 = 1.81 \pm 0.01$  and  $\Gamma_2 = 1.66 \pm 0.02$  for P1 and P2 respectively [39], whilst for MAGIC measurements [34] they are  $\Gamma_1 = 3.2 \pm 0.4$  and  $\Gamma_2 = 2.9 \pm 0.2$ . More extensive studies using the joint data of the *Fermi*-LAT satellite and the MAGIC telescope [19, 34] show that the spectrum follows a power law with an exponential cut-off lower limit of around  $\sim 700$  GeV. We have also performed a joint analysis using *Fermi*-LAT data and the LST-1 data together. We performed fits to two different models. First, a power law with a sub exponential cut-off (ECO):

$$\frac{d\Phi}{dE} = \Phi_0 \left( \frac{E}{E_0} \right)^{-\Gamma} \exp(-(\lambda E)^\alpha). \quad (5.2)$$

Second, a smooth broken power law (SBPL):

$$\frac{d\Phi}{dE} = \Phi_0 \left( \frac{E}{E_0} \right)^{-\alpha_1} \left( 1 + \left( \frac{E}{E_b} \right)^{\frac{\alpha_2 - \alpha_1}{\gamma}} \right)^{-\gamma}. \quad (5.3)$$

In Figure 5.3 we show the resulting for both models to each peak. From the figure we can see a smooth transition between the *Fermi*-LAT data and our LST-1 data.

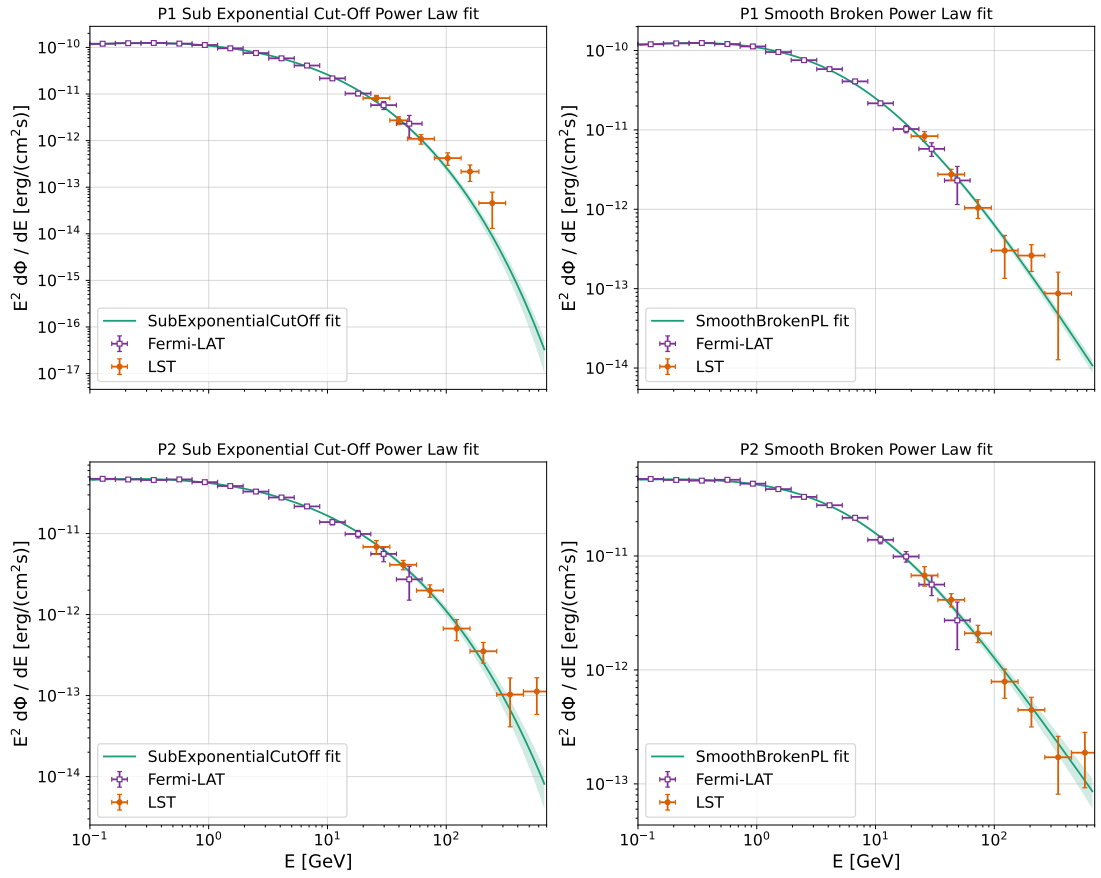


Figure 5.3: Joint fits for the joint *Fermi*-LAT and LST-1 data. Top left: Sub Exponential Cut-off for P1. Bottom left: Sub Exponential Cut-off for P2. Top right: Smooth Broken power law for P1. Bottom right: Smooth Broken power law for P2.

The resulting best-fit parameters from the fits above are summarized in Table 5.2.

ECO	$\Phi_0[\text{cm}^{-2} \text{s}^{-1} \text{TeV}^{-1}]$	$\Gamma$	$\lambda$	$\alpha$	AIC	
P1	$(4.3 \pm 0.08) \cdot 10^{-4}$	$1.57 \pm 0.03$	$5.46 \pm 1.8$	$0.363 \pm 0.016$	47	
P2	$(1.12 \pm 0.03) \cdot 10^{-4}$	$1.71 \pm 0.04$	$3.2 \pm 2$	$0.32 \pm 0.03$	48	
SBPL	$\Phi_0[\text{cm}^{-2} \text{s}^{-1} \text{TeV}^{-1}]$	$\alpha_1$	$\alpha_2$	$E_b[\text{GeV}]$	$\gamma$	AIC
P1	$(1.35 \pm 0.04) \cdot 10^{-4}$	$1.793 \pm 0.010$	$4.37 \pm 0.06$	$9.1 \pm 0.6$	$3.63 \pm 0.10$	40
P2	$(0.348 \pm 0.004) \cdot 10^{-4}$	$1.94 \pm 0.04$	$3.50 \pm 0.18$	$8 \pm 3$	$1.8 \pm 0.5$	44

Table 5.2: Fit parameters for both models tested in the joint *Fermi*-LAT and LST-1 analysis.

The Akaike Information Criterion (AIC) for Smooth Broken power law is lower for both peaks, meaning that this is the favoured one. The physical implications of both models are still being discussed, and it is expected that future data with improved the statistics in the higher energy bins will shed some light on the best-fit to the data.

## 5.2 Systematic errors

Following the procedure outlined in Section 4.2) we now present the systematic errors obtained for each parameter variation. In Tables 5.3 and 5.4 we can see the relative upper and lower error for each parameter and peak. The first noticeable tendency is that the errors for the reference flux is always higher than the error for the index. This is due to the reference flux depending on the number of events used for the fit, which in turn depends on how restrictive the cuts applied are. The spectral index is the parameter of greater importance as it is the one that contains the information on the acceleration mechanisms at play, if we recall 2.2.1 different mechanism have different indices. As such, the following discussion will be mainly focused on the errors of the spectral index.

For both peaks, we can see that the error due to variations in the intensity leakage cuts are the smallest ones. This means that this particular cut has little influence in the final results. This fact can be explained due to various reasons. First, we have to take into account that the cut in leakage intensity is a threshold, meaning that events are only discarded if they are above this threshold e.g. we discard events if their leakage is above a given value. There is not a fixed number of events that has to

Cut	$\Gamma$ upper	$\Gamma$ lower	$\Phi_0$ upper	$\Phi_0$ lower
Alpha containment	3%	4%	20%	21%
Gamma/Hadron Efficiency	1.6%	4%	21%	10%
Zenith distance	8%	0.4%	1.9%	42%
Intensity cut	7%	7%	44%	44%
Intensity leakage	0.3%	1.0%	6%	2.1%

Table 5.3: Relative errors on P1.

Cut	$\Gamma$ upper	$\Gamma$ lower	$\Phi_0$ upper	$\Phi_0$ lower
Alpha containment	1.7%	0.11%	1.6%	15%
Gamma/Hadron efficiency	1.6%	1.5%	4%	17%
Zenith distance	0.17%	1.2%	9%	1.9%
Intensity cut	2.0%	2.0%	6%	6%
Intensity leakage	0.3%	0.05%	0.3%	2.2%

Table 5.4: Relative errors on P2.

be discarded, in contrast with cuts like alpha containment of g/h efficiency where we forcibly remove a certain percentage of the events. This can explain why its error is lower in comparison. On the other hand, the leakage intensity tells us how close the detected shower is to the border of the camera. Images too close to the border (or even with part of the cascade not being inside the image), would have poor *gamaness* score meaning they would have either way been cut in other selection processes. Therefore, we can expect the data arriving to the cut in leakage to have low leakage values by default.

Another behaviour which stands out is the heavy asymmetry in the index error when changing the cut in zenith distance. For both peaks, one of the errors (upper for P1 lower for P2) is larger than the other. This means that cuts in one direction are much more influential than the other. In particular, for both peaks the larger error comes from lowering the zenith distance threshold. This means that most of the significant data comes from detections closer to the zenith. The further we go from the zenith, the less quality the data has. This is due to the fact that more zenith distance equals more air mass above the telescope, so the Cherenkov radiation has to travel larger distances in air and is more affected by attenuation. Ultimately this results in poorer detection and reconstruction of the cascade, so the data is more susceptible to

being discarded by other cuts.

For the spectral index error in both alpha containment and efficiency, there is no clear pattern to be discerned. In fact, both present slightly asymmetric errors in different peaks. This tells us that changes both lowering and rising the threshold for these cuts can introduce a significant systematic bias. This could mean that maintaining values close to the reference values may be optimal to obtain a balance between a higher number of events to have more solid statistic and fewer events but with better reconstruction. We also have to take into account that the cuts in efficiency and alpha containment are applied only to the IRFs, showing the influence they have on the final results.

A final comparison between the individual errors is that the cut in intensity has the highest relative error for both peaks. Higher energy cascades produce more photons, and thus their intensity is higher. As a result, applying a higher cut in intensity discards lower energy events while maintaining higher energy ones, in term producing a flattening of the index which is what we observe. To maintain maximum information, it could be better to maintain the cuts applied in the reference model, as those are the lowest possible based on the telescope performance. It has to be noted that, because two different cuts were applied to the data for the reference model, the calculated value may not be truly representative of the error this cut introduces. For data taken prior to August 2021 a intensity cut of 80 p.e. was applied, whilst for data taken after August 2021 (and for future detections) a cut of 50 p.e. is applied. As such, newer data will have a higher error in comparison to older data as their reference cut is further from the cut applied for the error calculation. This may give rise to an under-estimation of the uncertainty as we are using older data which has a lower error. Ideally, the importance of this cut could be revisited in the future when more data, which will have a cut of 50 p.e. is available.

In the Figure 5.4 we can see the reference model represented with the systematic error regions corresponding to each studied cut. These figures give us a good visual intuition about the importance of each cut. When comparing the width of the error band with the errors bars of the spectral nodes we can see which cuts and which energy ranges are more influential than the statistical errors of the data.

In Table 5.5 we show the errors associated with each node. This means, how far the SED computed with the events assigned to each individual node vary from the reference model. It has to be noted that a best-fit could not be obtained for all of the nodes because they did not have enough events for it to converge. The first notable

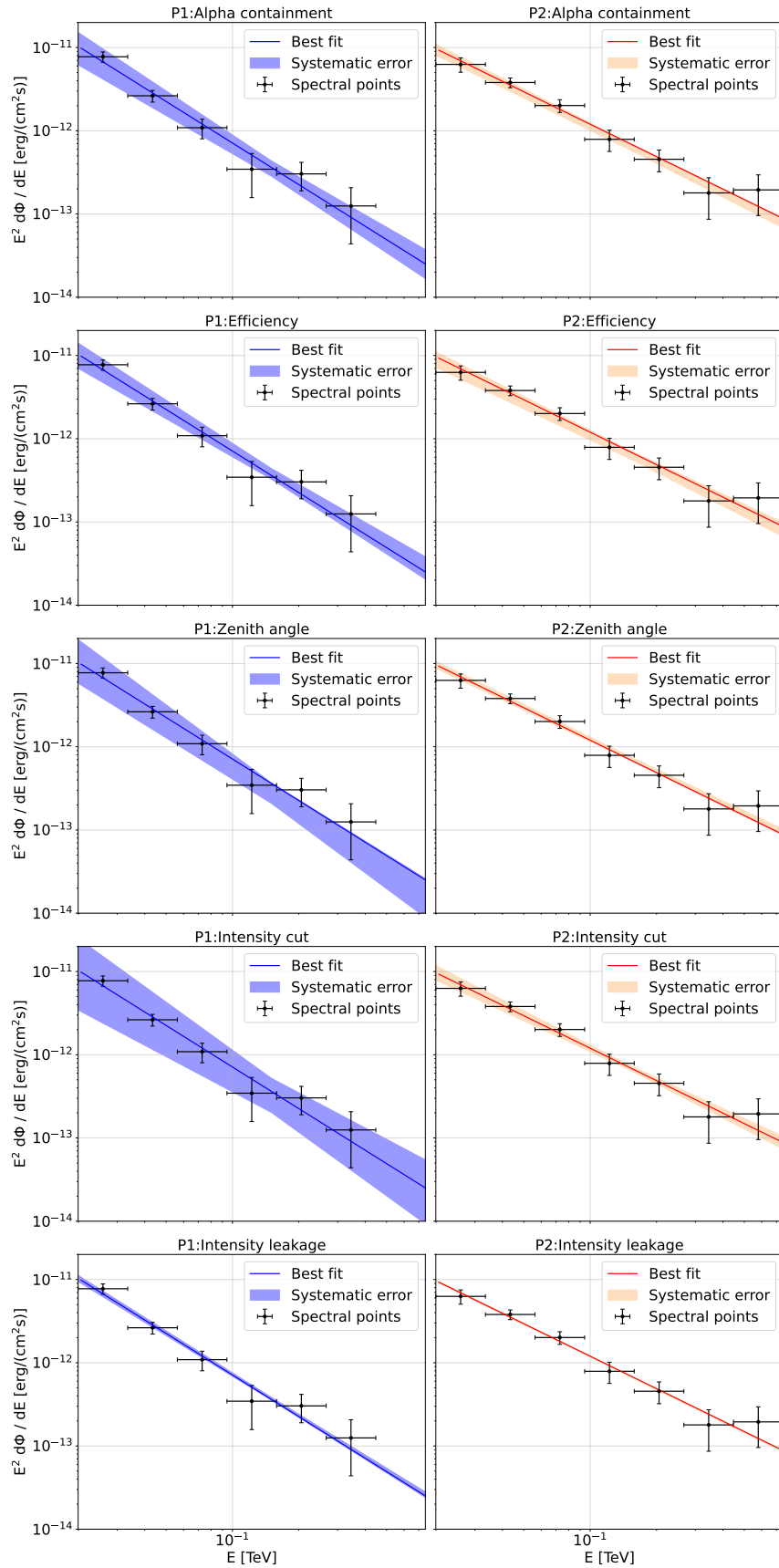


Figure 5.4: SED with error bands corresponding to each variation parameter studied, for P1 (left) and P2 (right).



feature common for both peaks is that nodes located closer to the zenith deviate less from the reference model. This agrees with what we discussed above regarding the cut in zenith distance, data closer to the zenith has lower energy threshold and thus is better reconstructed. Regarding the magnitude of the deviations, we can determine that even for the low zenith nodes the parameters deviate noticeably from the reference one.

In light of the errors obtained for the cuts in alpha containment, efficiency and the deviations per node, we can determine that the main source of systematic error is the process of applying the IRFs. This process starts by assigning the closest node to each event. This can create a bias in the sense that the IRFs are direction-dependent, but they are only computed along the directions of 12 nodes. As a consequence, the IRFs applied to the a event will not have the exact same direction as the event, which may lead to systematic errors. A solution to this problem could be calculating IRFs calculating the IRFs in a finer binning in the sky. The IRFs are also dependant on the MC simulations used so an improvement of the quality/number of simulations could reduce the systematic errors introduced when applying IRFs. Both of these possibilities would require huge computational cost. To reduce the cost and maximise the efficiency of the systematic error reduction, we can use our previous result that most of the significant data has been taken at low zenith distances, so the new testing nodes could be located near the zenith.

We have to remind ourselves that the IRFs are a measure of how the telescope itself can distort the data. Both the IRFs and the MC simulations depend on real measurements of the different telescope components. All these steps can introduce systematic errors that will propagate to the errors we calculated, and which can not be accounted for in the study here presented. As such, there will always be non-negligible systematic uncertainties in the final results despite the efforts to minimize them, and that will compete with the statistical deviations of the data.

The total systematic uncertainties are shown in Table 5.6. These final uncertainties we present completely characterize the systematic uncertainties introduced in the Crab Pulsar's spectrum during the data processing levels from the parameterized Cherenkov flash image up to the final stage of data processing. By analysing them we can determine that the data for P1 is more susceptible to biases introduced during the processing. This ties back to the fact that the overall statistic for P1 is worse than that of P2 as discussed above. We can expect the errors, specially for P1, to decrease with future data that improves the statistics.

Node	$\Gamma$ error	$\Phi_0$ error	Node	$\Gamma$ error	$\Phi_0$ error
2	4%	48%	1	6%	24%
3	11%	99%	2	1.4%	1.7%
4	17%	131%	3	8%	18%
6	13%	191%	4	3%	49%
7	93%	100%	5	114%	100%
9	15%	125%	6	5%	15%
10	16%	36%	8	29%	67%
13	16%	134%	13	7%	20%

(a) P1 (b) P2

Table 5.5: Per node errors for both peaks.

In Figure 5.5 we show the plot of the Spectral Energy Density best fit-models with their respective statistical error and the total systematic uncertainties added in quadrature. The striped region in the figure corresponds to the systematic effect of all of the different analysis parameters varied during the data processing chain. For both peaks, the error region due to systematic effects is always bigger than the statistical one. This means that the uncertainties in the results due to the different cuts made during the analysis are more significant than the fluctuations in the data.

Peak	$\Gamma$ upper	$\Gamma$ lower	$\Phi_0$ upper	$\Phi_0$ lower
P1	11%	9%	53%	65%
P2	3%	3%	12%	25%

Table 5.6: Final relative errors obtained after summing the errors introduced by each cut via quadrature.

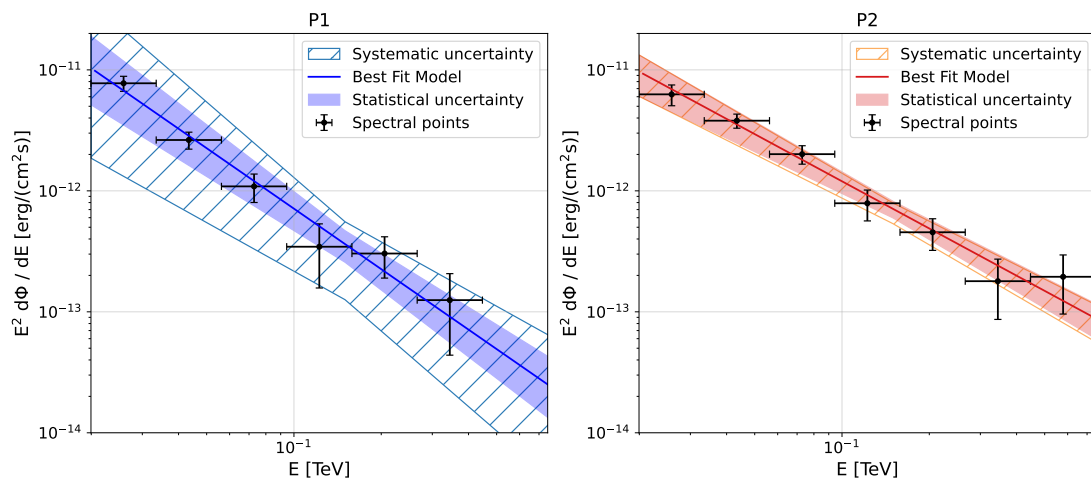


Figure 5.5: SED with statistical uncertainty (shaded) and final systematic error summing all contributions via quadrature (striped) for both peaks P1 (left) and P2 (right) of the Crab Pulsar.

## 6 | Conclusions

The conclusion of this master's thesis can be summed up as follows:

- We have successfully computed the systematic uncertainties introduced in the Crab Pulsar's spectrum by each of different cuts applied in the DL2 to DL4 data levels from the LST-1 telescope data processing chain. We have added these errors in quadrature into one final systematic error giving a characterization of the total systematic uncertainty introduced in said data levels.

To compute the uncertainties extensive data processing was required. Using the `cta-lstchain` software we processed data starting from the DL2 up to DL4 stage for both of the pulsar peaks for different values of the analysis parameters. In total, we generated nineteen different datasets. This includes not only the processing of the data taken by the telescope but also the generation of new Instrument Response Functions for each value of the parameters studied. After generating the DL4 datasets, we computed the Spectral Energy Distribution for all of them with the corresponding best-fit to a power law model. We estimated the systematic uncertainties by comparing the values of these fits to a *reference model*. This procedure yielded an upper and a lower uncertainty for the parameters of the best-fit model associated to each one of the five analysis parameters studied. The uncertainties introduced by each cut can be seen in Tables 5.3, 5.4, and in Figure 5.4 we show the reference model plotted with the error region corresponding to the uncertainty of each analysis parameters. We also computed the best-fit of the SED for each of the sky nodes used in the training of the IRFs for the reference data.

- By comparing the different uncertainties obtained, we discuss which analysis parameters introduce higher biases to the final results. In light of this discussion, we conclude that the highest source of uncertainty is the process of assigning

events to the different sky nodes and applying the associated IRFs. A possible solution to reduce this error could be a finer binning of the sky positions to increase the number of nodes, particularly in the low zenith region.

- All of the systematic uncertainties of each analysis parameter were added via quadrature to give an estimation of the total systematic uncertainty introduced in the Crab Pulsar's spectrum during data processing. We show the total systematic uncertainty Figure 5.5, where the *reference model* is plotted with its statistical errors and with the total systematic uncertainty. A comparison of both errors highlights the fact that the systematic uncertainty is always higher than the statistical one.
- We have also presented the final results obtained after the full analysis chain of the *reference model*. Both the phaseogram and the SED are consistent with the previous result on the Crab Pulsar. Using the reference data together with data from the *Fermi*-LAT telescope we performed additional fits over a wider range of energies for two different models. The transition between both data-sets is smooth and from the two models tested the Smooth Broken Power Law was the favoured one, although newer data is expected to shed light on the best-fit model.

Properly understanding the systematic uncertainties introduced during data processing is fundamental. Such uncertainties are inevitable, and knowing how each cut affects the final results allows for a finer tuning of their values as to maximize the quality of the end result. The errors presented in this thesis are a novelty study: we have computed the systematic uncertainties in the processing chain of one of the telescopes of the biggest upcoming collaboration in high energy astrophysics. The uncertainties obtained in this thesis will be part of a future publication by the LST-1 collaboration presenting the result obtained for the Crab Pulsar.

## 7 | Appendix: Statistical expressions.

Considering the number of events is a Poisson variable, the likelihood function used for the best-fit of the data is:

$$\ln [\mathcal{L}(S, B)] = n_{on} \ln[(S - \alpha B)T] + n_{off} \ln BT - [S + (\alpha + 1)B]T \quad (7.1)$$

Where:

- $n_{off}$  is the number of counts in the OFF or background region.
- $n_{on}$  is the number of counts in the ON or source region (without subtracting the background).
- $S$  is the source rate.
- $B$  is the background rate.
- $T$  is the total time of observation.
- $\alpha$  is the mean of the Poisson distribution. It is determined by the model that is being fit.

The statistical test for this likelihood expression is [40]:

$$TS = 2 \left[ n_{on} \ln \frac{(1 + \alpha)n_{on}}{\alpha(n_{on} + n_{off})} + n_{off} \ln \frac{(1 + \alpha)n_{off}}{n_{on} + n_{off}} \right] \sim \chi^2(1). \quad (7.2)$$

We use this value to compute the p-value of the fits according to a  $\chi^2(1)$  distribution. And the significance is:

$$\sigma = \sqrt{TS}. \quad (7.3)$$

The statistical test we use to compare models is the Akaike Information Criterion [41], given by:

$$AIC = 2k - 2 \log \mathcal{L}, \quad (7.4)$$

where  $k$  is the number of free parameters of the model and  $\log \mathcal{L}$  the value of the likelihood function for the best-fit parameters. In this test, the model with lower AIC is favored.

# Bibliography

- [1] *CTA official website*. <https://www.cta-observatory.org/about/how-ctao-works/>. Accessed: 23-07-2023.
- [2] A. Moralejo. “LST-1, the Large-Sized Telescope prototype of CTA. Status and first observations”. In: *Journal of Physics: Conference Series* 2156.1 (2021), p. 012089. DOI: 10.1088/1742-6596/2156/1/012089.
- [3] *Messier Catalogue: M1 information*. <https://www.messier-objects.com/messier-1-crab-nebula/>. Accessed: 15-07-2023.
- [4] M.S. Longair. *High Energy Astrophysics*. 3rd ed. Cambridge University Press, 2011. ISBN: 9780511778346.
- [5] <https://web.physics.utah.edu/~whanlon/spectrum.html>. Accessed: 23-07-2023.
- [6] J. Blümer, R. Engel, and J.R. Hörandel. “Cosmic rays from the knee to the highest energies”. In: *Progress in Particle and Nuclear Physics* 63.2 (2009), pp. 293–338. DOI: 10.1016/j.pnpnp.2009.05.002.
- [7] M. Kachelrieß and D.V. Semikoz. “Cosmic ray models”. In: *Progress in Particle and Nuclear Physics* 109 (2019), p. 103710. ISSN: 0146-6410. DOI: <https://doi.org/10.1016/j.pnpnp.2019.07.002>.
- [8] G. T. Zatsepin and V. A. Kuz'min. “Upper Limit of the Spectrum of Cosmic Rays”. In: *Soviet Journal of Experimental and Theoretical Physics Letters* 4 (1966), p. 78.
- [9] K. Greisen. “End to the Cosmic-Ray Spectrum?” In: *Phys. Rev. Lett.* 16.17 (1966), pp. 748–750. DOI: 10.1103/PhysRevLett.16.748.
- [10] *Wikipedia*. [https://es.m.wikipedia.org/wiki/Archivo:Pulsar\\_schematic.svg](https://es.m.wikipedia.org/wiki/Archivo:Pulsar_schematic.svg). Accessed: 27-07-2023.



- [11] G. Ceribella. “Insights into the 10-100 GeV gamma-ray emission of pulsars from extensive observations of MAGIC”. PhD thesis. Munich, Tech. U., 2021.
- [12] A. De Angelis and M.J. Pimenta Martins. *Introduction to particle and Astroparticle Physics: Multimessenger astronomy and its particle physics foundations*. Springer, 2018. ISBN: 978-3-319-78180-8.
- [13] K. Brecher, R. A. Fesen, S. P. Maran, and J. C. Brandt. “Ancient records and the Crab Nebula supernova”. In: *The Observatory* 103 (1983), pp. 106–113.
- [14] M. Meyer, D. Horns, and H.-S. Zechlin. “The Crab Nebula as a standard candle in very high-energy astrophysics”. In: *Astronomy & Astrophysics* 523 (2010). DOI: 10.1051/0004-6361/201014108.
- [15] M. C. Weisskopf, M. Guainazzi, K. Jahoda, et al. “On calibrations using the Crab Nebula and models of the nebular X-Ray emission”. In: *The Astrophysical Journal* 713.2 (2010), p. 912. DOI: 10.1088/0004-637X/713/2/912.
- [16] D. A. Kniffen, R. C. Hartman, D. J. Thompson, et al. “Gamma radiation from the Crab Nebula above 35 MeV”. In: *Nature* 251.5474 (1974), pp. 397–399. DOI: 10.1038/251397a0.
- [17] C. E. Fichtel, R. C. Hartman, D. A. Kniffen, et al. “High-energy gamma-ray results from the second Small Astronomy Satellite.” In: *The Astrophysical Journal* 198 (1975), pp. 163–182. DOI: 10.1086/153590.
- [18] L. Kuiper, W. Hermsen, G. Cusumano, et al. “The Crab pulsar in the 0.75-30 MeV range as seen by CGRO COMPTEL. A coherent high-energy picture from soft X-rays up to high-energy gamma-rays”. In: 378 (2001), pp. 918–935. DOI: 10.1051/0004-6361:20011256.
- [19] MAGIC Collaboration, E. Aliu, H. Anderhub, et al. “Observation of Pulsed Gamma-Rays Above 25 GeV from the Crab Pulsar with MAGIC”. In: *Science* 322.5905 (2008), pp. 1221–1224. DOI: 10.1126/science.1164718.
- [20] The VERITAS Collaboration, E. Aliu, T. Arlen, et al. “Detection of Pulsed Gamma Rays Above 100 GeV from the Crab Pulsar”. In: *Science* 334.6052 (2011), pp. 69–72. DOI: 10.1126/science.1208192.
- [21] MAGIC Collaboration, V. A. Acciari, S. Ansoldi, et al. “MAGIC very large zenith angle observations of the Crab Nebula up to 100 TeV”. In: *A&A* 635 (2020), A158. DOI: 10.1051/0004-6361/201936899.
- [22] <https://www.lst1.iac.es/photos.html>. Accessed: 23-07-2023.

- [23] CTA-LST project, H. Abe, A. Aguasca, and I. Agudo. “Physics Performance of the Large Size Telescope prototype of the Cherenkov Telescope Array”. In: *PoS ICRC2021* (2021), p. 806. DOI: 10.22323/1.395.0806.
- [24] CTA-LST project, H. Abe, et al. “Observations of the Crab Nebula and Pulsar with the Large-Sized Telescope Prototype of the Cherenkov Telescope Array”. In: (June 2023). arXiv: 2306.12960 [astro-ph.HE].
- [25] R. Lopez-Coto, T. Vuillaume, A. Moralejo, et al. *cta-observatory/cta-lstchain: v0.10.1 - 2023-07-07*. Version v0.10.1. 2023. DOI: 10.5281/zenodo.8124257.
- [26] <https://cta-observatory.github.io/cta-lstchain>. Accessed:31-08-2023.
- [27] A.M. Hillas. “Cerenkov Light Images of EAS Produced by Primary Gamma Rays and by Nuclei”. In: *19th International Cosmic Ray Conference (ICRC19), Volume 3*. Vol. 3. International Cosmic Ray Conference. 1985, p. 445.
- [28] *Jodrell Bank observatory:Crab Pulsar ephemeris*. <http://www.jb.man.ac.uk/~pulsar/crab.html>. Accessed: 23-07-2023.
- [29] A. G. Lyne, R. S. Pritchard, and F. Graham Smith. “23 years of Crab pulsar rotational history”. In: *Monthly Notices of the Royal Astronomical Society* 265.4 (1993), pp. 1003–1012. DOI: 10.1093/mnras/265.4.1003.
- [30] Á. Mas Aguilar. *PulsarTimingAnalysis: v0.2 - 2022-06-07*. Version v0.2. June 2022. URL: <https://github.com/alvmas/PulsarTimingAnalysis>.
- [31] C. Deil, R. Zanin, J. Lefaucheur, et al. “Gammapy - A prototype for the CTA science tools”. In: *35th International Cosmic Ray Conference (ICRC2017)*. Vol. 301. International Cosmic Ray Conference. 2017, 766, p. 766. arXiv: 1709.01751 [astro-ph.IM].
- [32] H.E.S.S. Collaboration, H. Abdalla, A. Abramowski, et al. “The H.E.S.S. Galactic plane survey”. In: *A&A* 612 (2018), A1. DOI: 10.1051/0004-6361/201732098.
- [33] Fermi-LAT collaboration, S. Abdollahi, F. Acero, et al. “Incremental Fermi Large Area Telescope Fourth Source Catalog”. In: *The Astrophysical Journal Supplement Series* 260.2 (2022), p. 53. DOI: 10.3847/1538-4365/ac6751.
- [34] MAGIC Collaboration, S. Ansoldi, L. A. Antonelli, et al. “Teraelectronvolt pulsed emission from the Crab Pulsar detected by MAGIC”. In: *A&A* 585 (2016), A133. DOI: 10.1051/0004-6361/201526853.
- [35] MAGIC Collaboration, J. Aleksić, S. Ansoldi, et al. “Detection of bridge emission above 50 GeV from the Crab pulsar with the MAGIC telescopes”. In: *A&A* 565 (2014), p. L12. DOI: 10.1051/0004-6361/201423664.

- [36] MAGIC Collaboration, J. Aleksić, E. A. Alvarez, et al. “Observations of the Crab Pulsar between 25 and 100 GeV with the MAGIC I Telescope”. In: *The Astrophysical Journal* 742.1 (2011), p. 43. DOI: 10.1088/0004-637x/742/1/43.
- [37] L. Kuiper, W. Hermsen, G. Cusumano, et al. “The Crab pulsar in the 0.75-30 MeV range as seen by CGRO COMPTEL - A coherent high-energy picture from soft X-rays up to high-energy s”. In: *A&A* 378.3 (2001), pp. 918–935. DOI: 10.1051/0004-6361:20011256.
- [38] CTA-LST project, A. A. Abdo, M. Ackermann, et al. “Fermi Large Area Telescope Observations of the Crab Pulsar and Nebula”. In: *The Astrophysical Journal* 708.2 (2009), pp. 1254–1267. DOI: 10.1088/0004-637x/708/2/1254.
- [39] K. K. Madsen, S. Reynolds, F. Harrison, et al. “Broadband X-ray Imaging and Spectroscopy of the Crab Nebula and Pulsar with NuSTAR”. In: 801.1, 66 (2015), p. 66. DOI: 10.1088/0004-637X/801/1/66. arXiv: 1502.07765 [astro-ph.HE].
- [40] T. -P. Li and Y. -Q. Ma. “Analysis methods for results in gamma-ray astronomy.” In: *The Astrophysical Journal* 272 (1983), pp. 317–324. DOI: 10.1086/161295.
- [41] H. Akaike. “A new look at the statistical model identification”. In: *IEEE Transactions on Automatic Control* 19.6 (1974), pp. 716–723. DOI: 10.1109/TAC.1974.1100705.